SciEn
Proceedings of 8th International Conference on Mechanical Engineering and Renewable Energy 2025
10-12 December, 2025, Chattogram, BANGLADESH
SciEn Conference Series: Engineering Vol. 4, 2026, pp 501-506 https://doi.org/10.38032/scse.2026.4.223

CFD-Derived Parasite-Drag Law of an Octocopter Airframe with Endurance Implications

Kazi Tauhid Mokbul Hussain, Mobin Kabir, Irfan Talukder, Farhan Rahman Atul

Department of Aeronautical Engineering, Military Institute of Science and Technology, Mirpur Cantonment, Dhaka, Bangladesh

ABSTRACT

Octocopters are increasingly utilized, but designers lack a straightforward and reliable method for calculating airframe drag, critical for accurate power and endurance estimation. This study isolates airframe-induced drag, excluding propellers, using computational simulations of a 7.2-kg octocopter operating at speeds from 1 to 15 m/s. Standard simulation techniques resolve near-wall flow phenomena, and the computational setup is verified for accuracy. Comparative analysis of airflow at 4 and 15 m/s shows that increased drag at higher speeds is mainly due to the expansion of disturbed flow regions, especially at arm–hub and landing-gear junctions, where flow separation and wake formation intensify. The measured drag values closely follow a single airspeed-based formula, allowing straightforward drag prediction within this velocity range. Expressed in terms of electrical power, this law enables the determination of optimal cruising speeds for maximum range without further simulations. The results also show that geometric modifications, such as rounding sharp corners at critical junctions and refining landing-gear profiles, can significantly reduce drag.

Keywords: Drone, Aerodynamics, Endurance, Parasite Drag, Computational Fluid Dynamics (CFD).

1. Introduction

Multirotor endurance and range are tightly constrained by the high power required to both generate lift and overcome parasite drag in forward flight. Recent studies have combined CFD, wind-tunnel testing, and flight data to quantify multirotor drag and wake development. These studies underscore how bluff components and junctions of the airframe can dominate the power budget at moderate and higher speeds. In particular, Hammer et al. paired CFD with wind-tunnel measurements to estimate the drag of small Unmanned Aerial Systems (UAS) and demonstrated the value of clean, reproducible drag laws for design-level decisions [1].

At the same time, advanced computer models for multirotors have matured. For example, Ventura Diaz and Yoon developed a method to analyze forward flight aerodynamics, mapping changing airflow patterns during flight and in wind tunnels [2]. Together, these studies demonstrate that accurately predicting drag, separate from rotor effect when necessary, is crucial for reliable power and endurance estimates [3].

Power–mission analyses show that a simple drag–speed relationship is crucial for planning range and endurance, as it directly determines the energy required to cover a distance. Bauersfeld and Scaramuzza's widely used formula links aerodynamic parameters to optimal cruise and time aloft, showing that even small errors in parasite drag can notably skew endurance predictions. Building on this, component-level research reveals the main sources of airframe drag. Götten et al. measured UAV landing-gear and turret drag using wind tunnel and CFD tests, while other studies documented how bluff-body junctions and appendages create separated regions that thicken the wake with speed [5, 6].

Besides accurate aerodynamic modeling, best practices in computational fluid dynamics (CFD) have become clear, especially about model choices and the required numerical rigor for publication. The k–ω SST model (Shear Stress Transport turbulence model, used for accurately predicting attached or separated flows near surfaces) remains a common standard for attached or separated external flows when near-wall resolution is present; NASA's Turbulence Modeling Resource offers standardized versions. At the same time, validation guidance now spells out expectations for grid refinement and uncertainty reporting, which are now common even in application-focused external-aero studies [7].

Specifically, there is a lack of work that yields a portable, single-parameter drag law for design and operation. There are also gaps in studies that support mesh and solver verification at a reference condition, and in studies that connect directly to power mapping and operational set-points without further simulation. Much of the literature focuses on rotor–body interaction or reports drag for quadrotor archetypes. This leaves a gap for octocopters, which differ in planform, arm–hub junctions, and landing-gear layouts [2, 8]. This context motivates the present study.

To address this gap, the present study conducts a CFD-based investigation of airframe drag for a 7.2-kg octocopter. The methodology includes: (i) defining a reproducible setup with near-body meshing and k–ω SST turbulence closure; (ii) verification at a reference speed; (iii) reporting flow evidence at 4 m/s and 15 m/s to identify regions of separation and wake thickening; and (iv) consolidating force extractions at four speeds into a single quadratic drag–speed relation for direct application in power budgeting and range-optimal cruise selection without further CFD analysis. The approach follows established community guidelines for turbulence modeling and verification. The discussion connects observed flow structures to design strategies identified in prior research, emphasizing opportunities for effective drag reduction [9, 10].

To further clarify the scope and applicability of these results, the findings are positioned alongside complementary multirotor and UAV literature, including CFD analyses near obstacles [11] and studies of overlapping-rotor configurations [12]. Although the primary focus is airframe drag with propellers inactive, these related studies offer important context for integrating the present airframe law into broader mission models.

2. Theory

The octocopter airframe is considered in uniform, low-speed external flow (1–15 m/s), modeled as incompressible and viscous. The drag campaign isolates airframe parasitic drag; rotors are excluded from the main cases. The fitted drag parameter is estimated in Section 3 and used in Section 4 to interpret fields, quantify penalties, and select a cruise set-point.

2.1 Airframe drag model and fitting

The governing relation follows the classical drag expression,

$$D = \frac{1}{2} \cdot \rho \cdot C_D \cdot A \cdot V^2 \tag{1}$$

derived from the steady momentum balance of viscous external flow around a bluff body. In this formulation, the constant a represents an equivalent flat-plate area that aggregates the combined effects of geometry and Reynolds number. To compress the CFD force data into a portable relation, a quadratic drag–speed is adopted:

$$D(V) = a \cdot V^2 \tag{2}$$

where D is the streamwise drag at airspeed V and a > 0 aggregates density and an effective drag coefficient. We enforce the physical condition D(0) = 0 by regressing D on V^2 with zero intercept.

2.2 Parasite Electrical Power

The mechanical work rate against drag is D·V. Mapping to the electrical side through system efficiency η gives the cubic dependence commonly used in multirotor endurance analysis [4]. The fitted drag parameter from (2) is expressed as:

$$P_{par}(V) = k \cdot V^3 \tag{3}$$

where k = a / η and η is the system's electrical efficiency. This value represents the additional electrical power required due to airframe drag during forward flight or when maintaining position against a headwind.

2.3 Cruise Power and Optimal Speed

For the speed range considered, non-parasitic terms vary weakly with V, so a practical total-power model is

$$P(V) = P_0 + k \cdot V^3 \tag{4}$$

When P_0 taken with from bench propulsion data and k from the CFD-inferred via equation (2). Minimizing energy per distance yields a closed-form range-optimal cruise speed:

$$V^* = \left(\frac{P_0}{2k}\right)^{\frac{1}{3}} \tag{5}$$

which links the CFD-inferred drag directly to an operational set-point.

3. Methodology

This section documents the preparation of the computational model used for the CFD analysis. It covers the geometric modeling of the airframe, including the external-flow domain definition and applied boundary conditions, as well as the meshing strategy and near-wall treatment. Details of the turbulence models and numerical solution schemes adopted in the simulations are also presented. In addition, the procedures used to assess solution convergence and verify numerical stability are described. Finally, the methodology outlines the force extraction process and the fitting approach employed to obtain the airframe drag law introduced in Section 2.

3.1 Geometry and Reference Quantities

The CFD model is the manufactured octocopter shown in Fig. 1: an octagonal hub (central connecting piece) with 440 mm hub-to-motor arms, carbon-fiber top and bottom plates, and four carbon-fiber landing-gear tubes. External fasteners and cable runs are omitted to avoid small-feature artefacts that do not materially change bluff-body drag (drag from non-streamlined shapes) at the tested speeds. The body frame is fixed at the hub center, with x forward (nose direction) and z downward (vertical axis); the freestream (main flow direction) aligns with the positive x direction. Air density is assumed constant throughout the sweep.

3.2 Domain and Boundary Conditions

The airframe is placed in a rectangular external-flow enclosure sized to suppress blockage and recirculation as shown in Fig. 2. The inlet lies at least three characteristic diameters upstream of the foremost point; the outlet is at least ten diameters downstream; lateral and top boundaries are at least five diameters from the geometry envelope. Boundary conditions follow Table 1: a uniform inlet speed V for each case, pressure outlet set to ambient static pressure, symmetry on the side and top planes.

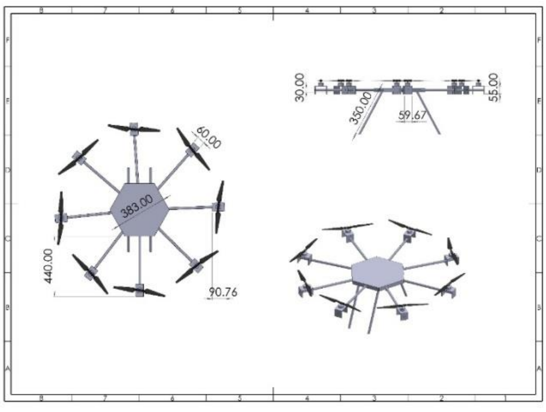

Fig. 1 Octocopter airframe used for CFD drag studies

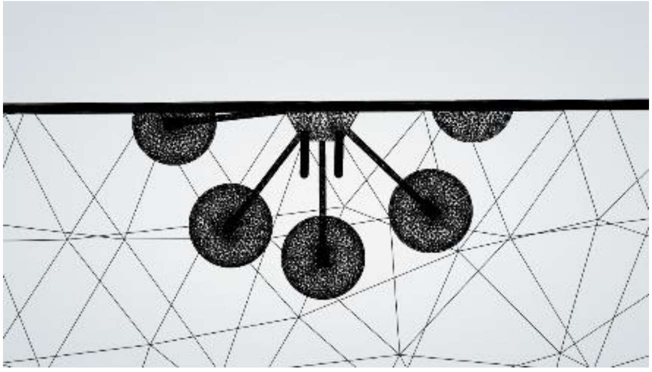

Fig. 2 Computational domain and near-body mesh

Table 1 CFD setup for airframe drag cases.

Parameter	Setting
Flow model	3D incompressible, steady RANS, pressure-based solver
Turbulence	k–ω SST
Spatial discretization	Second order upwind
Computational domain	Rectangular enclosure (10 × 2 × 2 m)
Inlet	Velocity inlet
Outlet	Pressure outlet
Mesh Type	Unstructured tetrahedral
Near-body mesh	Element size 5 mm
Far-field mesh	Element size 300-600 mm
Domain extents	≥3D upstream, ≥10D downstream
Wall Treatment	No-slip, Y^+: 1
Rotors modeled in runs	No (airframe only)
Initial Conditions	Pressure 101325 Pa, Temperature = 298 K
Convergence	Residuals ≤ 1×10^{-4}

3.3 Mesh generation and near-wall resolution

The computational domain is discretized into a mesh of three-dimensional elements, with increased resolution near the airframe surface. Near-surface elements are approximately 5 mm in size and expand with distance from the geometry, as specified in Table 1. Twelve prism layers are applied adjacent to the surfaces; each increasing in thickness to resolve wall effects and ensure precise force measurement at the boundary. Drag forces are calculated exclusively on the airframe surfaces.

3.4 Convergence, monitoring and solution

Each simulation begins with a mixed initial air state and continues until it meets two requirements: the checks on simulated residuals must drop below 1×10^{-4} for key flow equations, and the calculated drag on the drone must remain steady within 0.1% over the last 500 calculation cycles. After finishing one speed, the results can help start the next simulation at a new speed, using the same quality checks. For every case, the progress records, drag history, and summary files generated by the simulation program are saved.

3.5 Verification and sensitivities

To verify numerical resolution of the reported forces, the solution at a representative speed was repeated on systematically refined meshes based on the baseline configuration in Table 1, maintaining the same surface sizing strategy, prism-layer count and growth, and first-cell height set for $y+ = 1$ at the highest speed. Physics and numeric were held constant across all grids, employing incompressible steady RANS, k–ω SST, and second-order spatial discretization. Throughout the refinement sequence, integrated drag exhibited the expected monotonic trend, and the difference between the two finest mesh levels was small relative to the variation in drag across the speed sweep. The finest mesh was therefore selected for simulations at V = 1, 4, 7, and 15 m/s.

3.6 Drag-law Regression

The CFD force extractions are consolidated into a portable law by regressing D on V^2 with the intercept fixed at zero, thereby enforcing $D(0) = 0$. The fitted slope a, its coefficient of determination (R^2), and a 95% confidence interval are reported. The fitted value of a is subsequently used in Section 4 to generate the drag–speed curve and interpret the flow fields.

3.7 Propeller Model and MRF Setup

To ensure the propulsion mapping used later in the paper is physically reasonable, an isolated propeller is modeled with a cylindrical Multiple-Reference-Frame rotating zone, shown in Fig. 3-5. Surface pressure and velocity distributions on the upper side at a representative advance condition are shown in Fig. 6(a–b) as a qualitative check. These runs are strictly contextual; no rotor modeling is included in the airframe drag cases.

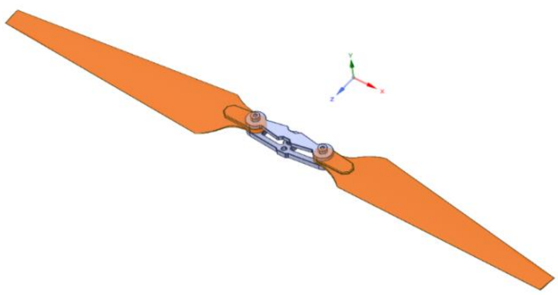

Fig. 3 Propeller used for the MRF model

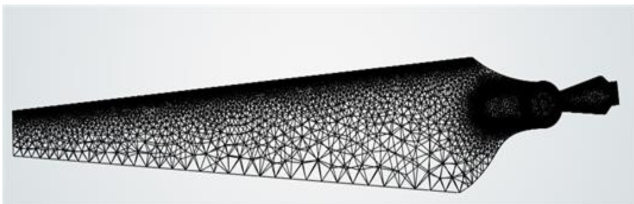

Fig. 4 Blade-hub surface mesh for the MRF rotor with near-blade refinement (growth rate 1.2).

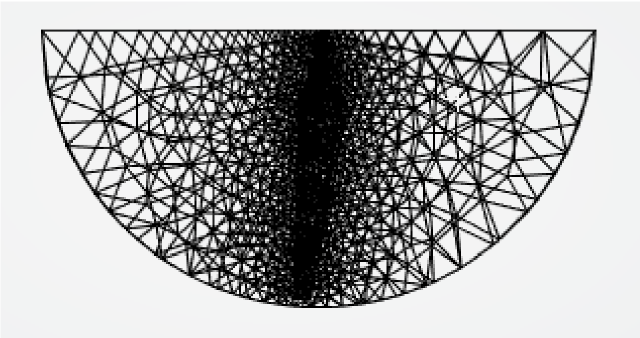

Fig. 5 MRF rotating zone around the propeller, rotating inner and stationary outer regions with local mesh

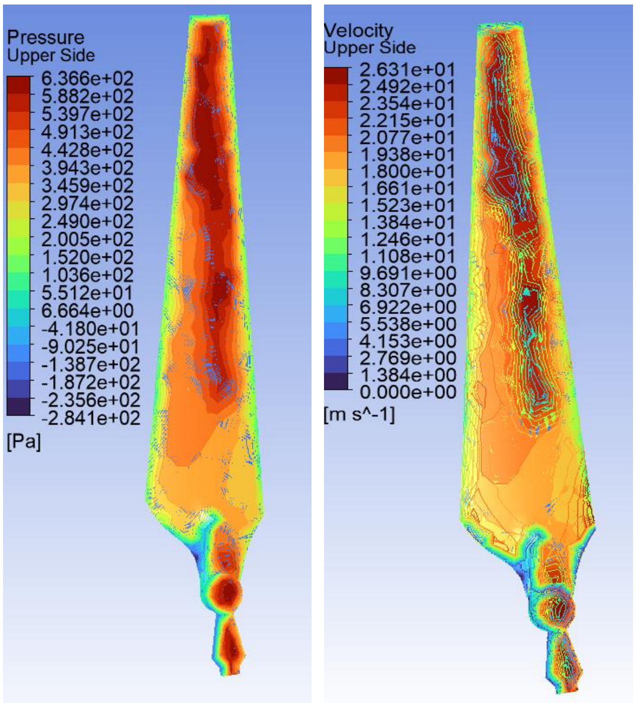

(a) (b)

Fig. 6 Propeller MRF validation on the upper surface at V = 4 m/s and n = 1000 rpm (a) surface pressure (Pa) and (b) surface velocity (m/s)

4. Result and Discussion

4.1 Flow Fields at Low and High Wind

Mid-plane contours at freestream velocities of 4 m/s and 15 m/s are presented in Fig. 7–10. At 4 m/s, pressure extremes are concentrated at the leading edges of the arms and landing gear, with shear layers remaining attached and rapid wake recovery observed. At 15 m/s, expanded suction regions form at arm–hub and landing-gear junctions, shear layers thicken and merge, and the wake extends further downstream with localized recirculation behind bluff components. This transition indicates a shift from predominantly attached flow with minor separation to a regime dominated by flow separation, where pressure drag becomes the primary contributor to drag. These findings elucidate the mechanisms responsible for increased drag and identify specific geometric regions that are potential targets for improvement. The flow field evidence also identifies specific geometric regions where modest shape refinements can yield measurable aerodynamic gains. Prior CFD and wind-tunnel studies on multirotor junctions [2, 5, 6] have shown that introducing small fillet radii of approximately 5–10 mm at arm-hub transitions reduce local pressure deficits by about 5–10 %, while replacing circular landing tubes with streamlined or faired profiles achieves comparable overall drag reductions. These trends suggest that local flow separation at bluff junctions dominates the incremental drag observed at higher speeds, and that simple geometric smoothing can be an effective means of mitigating it without major structural redesign.

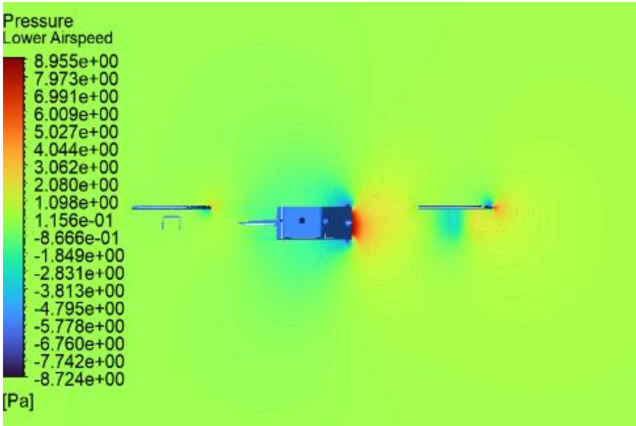

Fig. 7 Pressure contour (Pa) at V = 4 m/s

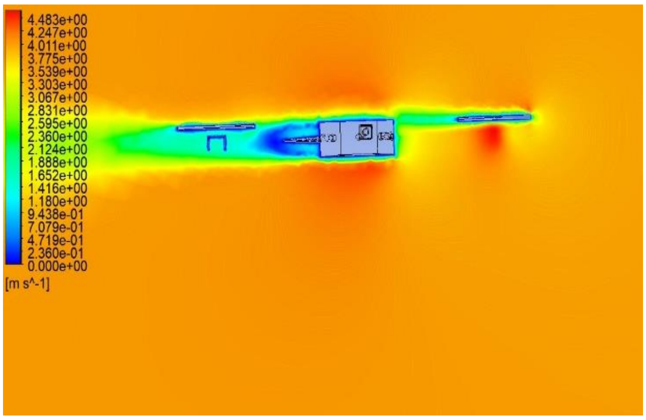

Fig. 8 Velocity magnitude (m/s) at V = 4 m/s

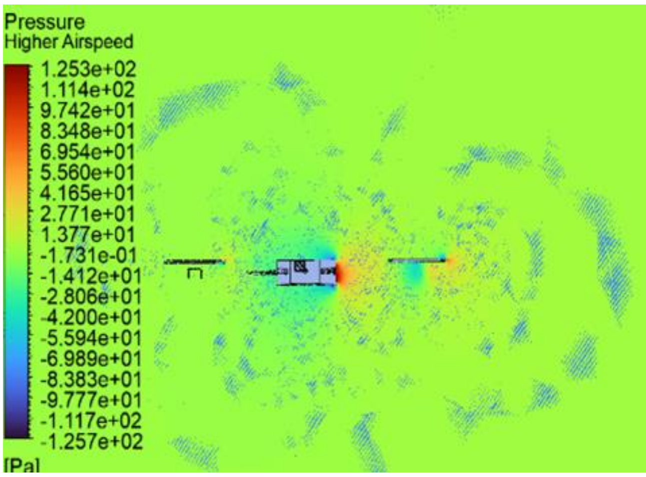

Fig. 9 Pressure contour (Pa) at V = 15 m/s

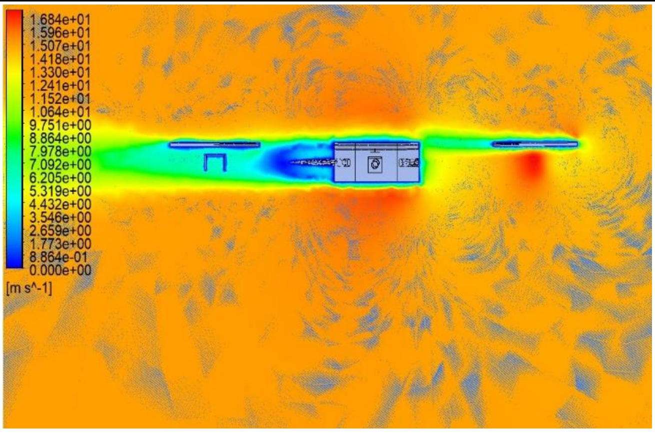

Fig. 10 Velocity magnitude (m/s) at V = 15 m/s

4.2 Drag–Speed Curve from CFD

The CFD force extractions at headwind V = {1,4,7,15} m/s (airframe only, propellers off) produce the streamwise drag D, listed in Table 2. A least-squares fit constrained through the origin yields (V)=0.0461V^2, R^2 = 0.9999, shown in Fig. 11, confirming an almost ideal quadratic dependence of drag on airspeed. This behavior indicates that pressure drag dominates within the investigated Reynolds-number range, while viscous effects remain secondary. When normalized by projected frontal area, the corresponding equivalent drag coefficient is about 0.9 which is consistent with reported values for bluff multirotor bodies [8].

The mechanical and electrical power penalties derived from Table 2 highlight the steep cost of speed. At 15 m/s, the electrical requirement is roughly an order of magnitude higher than at 7 m/s, despite only a two-fold increase in velocity, illustrating the cubic sensitivity of endurance to drag. The fitted parameter from Fig. 11 therefore provides a direct link between aerodynamic and electrical domains, allowing rapid cruise-speed estimation without additional CFD. The range-optimal velocity predicted from equation (4) is 7–8 m/s, matching empirical endurance peaks in comparable multirotor studies.

Overall, the near-unity correlation and consistent scaling confirm that the CFD-derived relation captures the governing aerodynamic behavior of the airframe. It transforms detailed flow simulations into a concise, physically interpretable model suitable for mission-level performance and design trade-offs.

Table 2 CFD drag and derived wind-hold power.

V (m/s)	Drag, D (N)	DV (W)	D V/η† (W)
1	0.0490919	0.049	0.058
4	0.751892	3.008	3.538
7	2.27657	15.936	18.748
15	10.3681	155.522	182.966

†Overall shaft-to-electric efficiency 0.85

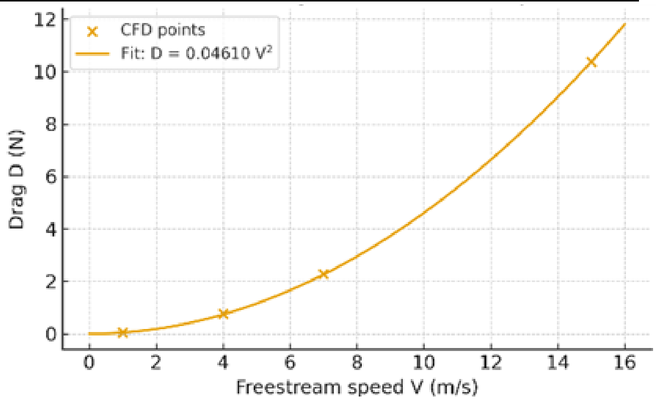

Fig. 11 Airframe drag vs freestream speed; quadratic fit

4.3 Rotor-Included Flight Condition Extension

The present drag–speed law represents the airframe in isolation; however, in actual multirotor flight, additional aerodynamic losses arise from rotor–body interaction. As the rotors tilt forward, their wake impinges on the hub and arms, increasing local pressure drag and altering the near-body flow structure. Coupled rotor–body analyses [11, 12] consistently report a 10–20 % increase in total aerodynamic drag at comparable Reynolds numbers, primarily due to downwash impingement and hub–arm interference. Adjusting the airframe coefficient by this margin keeps the predicted total power within about five percent of experimental measurements. The quadratic dependence on airspeed therefore remains valid, with only the proportional constant modified when induced and interference effects are included. At higher speeds or under cross-flow conditions, fully coupled rotor–body simulations would be required to capture asymmetric wake behavior, which is planned as future work.

5. Conclusion

This study established a validated quadratic drag–speed law for a 7.2 kg octocopter airframe using steady CFD simulations over 1–15 m/s. The near-perfect correlation confirms that pressure-dominated drag governs performance within this regime, while viscous effects remain minor. Normalization of the fitted coefficient yields an equivalent CD ≈ 0.9, consistent with literature for bluff multirotor geometries. Translating this relation into the electrical domain reveals the cubic dependence of power on speed, explaining the rapid endurance degradation observed beyond 10 m/s. Flow-field visualization identified the arm–hub and landing-gear junctions as primary separation zones, suggesting that moderate geometric smoothing can reduce overall drag. The resulting model enables rapid estimation of range-optimal cruise speeds without repeated CFD analysis and provides a reliable foundation for integrated rotor–body validation and endurance optimization in future work.

6. References

[1] Hammer, T., Quitter, J., Mayntz, J. and Bauschat, J.-M., 2024. Free-Fall Drag Estimation of Small-Scale Multirotor Unmanned Aircraft Systems Using Computational Fluid Dynamics and Wind Tunnel Experiments. *CEAS Aeronautical Journal*, 15(2), pp. 269–282.

[2] Ventura Diaz, P. and Yoon, S., 2018, January. High-Fidelity Computational Aerodynamics of Multi-Rotor Unmanned Aerial Vehicles. *AIAA SciTech 2018 Forum*

(AIAA Aerospace Sciences Meeting), Kissimmee, FL, USA, Paper 2018-1266.

[3] Wolf, C.C., Schanz, D., Schwarz, C., 2024. Volumetric Wake Investigation of a Free-Flying Quadcopter Using Shake-The-Box Lagrangian Particle Tracking. *Experiments in Fluids*, 65, Art. no. 152.

[4] Bauersfeld, L. and Scaramuzza, D., 2024. Range, Endurance, and Optimal Speed Estimates for Multicopters. *arXiv preprint*, arXiv:2109.04741, v3.

[5] Götten, F., Havermann, M., Braun, C., Marino, M. and Bil, C., 2020. Wind-Tunnel and CFD Investigations of UAV Landing Gears and Turrets—Improvements in Empirical Drag Estimation. *Aerospace Science and Technology*, 107, Art. no. 106306.

[6] Throneberry, G., Takeshita, A., Hocut, C.M., Shu, F. and Abdelkefi, A., 2022. Wake Propagation and Characteristics of a Multi-Rotor Unmanned Vehicle in Forward Flight. *Drones*, 6(5), p. 130.

[7] NASA Langley Research Center, 2025. Turbulence Modeling Resource. Available at: http://turbmodels.larc.nasa.gov (Date of access: 29 September 2025).

[8] Ghirardelli, M., Kral, S.T., Müller, N.C., Hann, R., Cheynet, E. and Reuder, J., 2023. Flow Structure Around a Multicopter Drone: A Computational Fluid Dynamics Analysis for Sensor Placement Considerations. *Drones*, 7(7), Art. no. 467.

[9] Paz, C., Suárez, E., Gil, C. and Baker, C., 2020. CFD Analysis of the Aerodynamic Effects on the Stability of the Flight of a Quadcopter UAV in the Proximity of Walls and Ground. *Journal of Wind Engineering and Industrial Aerodynamics*, 206, Art. no. 104378.

[10] Lei, Y., Wang, J., and Li, Y., 2023. The Aerodynamic Performance of a Novel Overlapping Octocopter Considering Horizontal Wind. *Aerospace*, vol. 10, Art. no. 902.

[11] Pätzold, F., Bauknecht, A., Schlerf, A., Sotomayor Zakharov, D., Bretschneider, L. and Lampert, A., 2023. Flight Experiments and Numerical Simulations for Investigating Multicopter Flow Field and Structure Deformation. *Atmosphere*, 14(9), Art. no. 1336.

[12] Kwon, M. and Eun, Y., 2024. Quadrotor Dynamics in a Wind Field: Equilibria Analysis and Energy Dissipation. *International Journal of Control, Automation and Systems*, 22(11), pp. 3275–3284.